

Article

Solvothermal Treatment of Micron-Sized Commercial $\text{SrAl}_2\text{O}_4:\text{Eu}^{2+}$, Dy^{3+} Phosphors and One-Step Preparation of Nanophosphors for Fingerprint Imaging

Rungang Liu, Xueting Liu, Weikai Lin and Yingliang Liu * 

College of Materials & Energy, South China Agricultural University, Guangzhou 510642, China; sliurg@163.com (R.L.); 14718595704@163.com (X.L.); lwk301130@163.com (W.L.)

* Correspondence: tliuyl@scau.edu.cn

Abstract: Preparing submicron and nanoscale phosphors with good optical properties for practical applications is a challenging task for current inorganic long afterglow luminescent materials. This study utilized commercialized $\text{SrAl}_2\text{O}_4:\text{Eu}^{2+}$, Dy^{3+} phosphors (SAOED) as raw materials and employed solvents with lower polarity or non-polar solvents for dynamic solvothermal treatment. The commercialized phosphor's overall average particle size was reduced from 42.3 μm to 23.6 μm while maintaining the fluorescence intensity at 91.39% of the original sample. Additionally, the study demonstrated the applicability of the dynamic solvothermal method to most other commercialized inorganic phosphors. The experiment produced a high-brightness nano-sized phosphor with a yield of 5.64%. The average diameter of the phosphor was 85 nm, with an average thickness of 16 nm. The quantum efficiency of the phosphor was 74.46% of the original sample. The fingerprint imaging results suggest that the nano-sized phosphors have potential for practical applications.

Keywords: solvothermal treatment; commercial phosphors; top-down; particle size; optical properties; nanophosphor



Citation: Liu, R.; Liu, X.; Lin, W.; Liu, Y. Solvothermal Treatment of Micron-Sized Commercial $\text{SrAl}_2\text{O}_4:\text{Eu}^{2+}$, Dy^{3+} Phosphors and One-Step Preparation of Nanophosphors for Fingerprint Imaging. *Appl. Sci.* **2024**, *14*, 3929. <https://doi.org/10.3390/app14093929>

Academic Editor: Francesco Enrichi

Received: 16 April 2024

Revised: 28 April 2024

Accepted: 2 May 2024

Published: 4 May 2024



Copyright: © 2024 by the authors. Licensee MDPI, Basel, Switzerland. This article is an open access article distributed under the terms and conditions of the Creative Commons Attribution (CC BY) license (<https://creativecommons.org/licenses/by/4.0/>).

1. Introduction

Micron-sized inorganic long afterglow luminescent materials are widely used in commercial products due to their excellent afterglow properties. Sustained luminescence is a unique optical process in which the luminescent material continues to emit a long-lasting afterglow after the end of excitation [1–3] and thus is widely used in security marking and night vision displays [4]. It is due to their excellent optical and afterglow properties that afterglow materials are currently playing an indispensable role in applications such as optical imaging and treatment of tumors [5,6], information anti-counterfeiting [7–9] and multiple encryption [10–12], photocatalysis [13], fingerprinting, bio-imaging [14], photovoltaic sensing [15–20], and light-emitting diodes [21].

Inorganic phosphors, especially those doped with rare earths, transition metals, and main group metals, show unique advantages in high stability, long afterglow time, tunable luminescence color (broad band from UV to IR), and high photoluminescence quantum yield (PLQY) due to the unique electronic structure of dopant ions. Since the discovery of long-afterglow luminescence at the beginning of the 20th century, great progress has been made in the development of long-afterglow materials. They have been rapidly developed in the past decade, and as a result, doped inorganic luminescent materials have been widely reported. Such as the well-known $\text{ZnGa}_2\text{O}_4:\text{Cr}^{3+}$, $\text{SrAl}_2\text{O}_4:\text{Eu}^{2+}$, Dy^{3+} , $\text{Zn}_2\text{GeO}_4:\text{Mn}^{2+}$, and the newly discovered $\text{CsPbBr}_3:\text{La}^{3+}$ [22–25]. In addition, more and more persistence has been reported, encouraged by the rapid development of synthesis techniques and precision optical instruments. Significant progress has been made in the exploration of the composition of persistent luminescent materials, persistent luminescent properties, working principles, and modulation methods [26–30]. Micrometer-scale inorganic long

afterglow luminescent materials are even more widely used in commercial products because of their excellent afterglow properties.

$\text{SrAl}_2\text{O}_4:\text{Eu}^{2+}, \text{Dy}^{3+}$ is a representative of inorganic long afterglow luminescent materials, first synthesized by Matsuzawa in 1996, which has several outstanding advantages: stability, high efficiency, and less toxicity [31]. However, the current production process of commercial $\text{SrAl}_2\text{O}_4:\text{Eu}^{2+}, \text{Dy}^{3+}$ is based on solid-phase reaction [32–37], which leads to poor homogeneity and product grain size in the micrometer range, thus limiting the practical application of $\text{SrAl}_2\text{O}_4:\text{Eu}^{2+}, \text{Dy}^{3+}$ phosphors in fields such as bioimaging, biomedicine, and fine chemicals. However, with the advancement of industrial and medical technologies, there is an urgent need for nanophosphors with good optical properties, uniform particles, and controllable morphology [17,38].

In this work, we select low-grade or non-polar alkane solvents to treat commercial $\text{SrAl}_2\text{O}_4:\text{Eu}^{2+}, \text{Dy}^{3+}$ phosphors by the stirring solvent heat method to maximize the protection of optical and afterglow properties, as well as verify the general applicability of this work. At the same time, a certain amount of sub-micron and nano-sized phosphors with good afterglow properties were prepared and extracted in this work. Compared with other top-down techniques such as mechanical milling, wet milling, laser ablation, etc., this work was easy to operate, the product still maintains good optical properties, and it can be simply dispersed without agglomeration, which is conducive to practical applications. In addition, the reaction solvent can be recycled after the reaction, which is not only resource-saving but also environmentally friendly, in line with the theme of green chemistry nowadays.

2. Materials and Methods

A turbid liquid was formed by dispersing 10 g of 40 μm commercial SAOED (Original) in 250 mL of cyclohexane solvent. The mixture was then stirred for 3 h and ultrasonicated for 10 min. Next, the mixture was transferred to a 1 L reactor and stirred by adding a magnet at 150 $^\circ\text{C}$ for 24 h. After the reaction was complete, the reactor was removed, and the product was collected by centrifuging the precipitate at 8000 rpm for 10 min. The precipitate was collected and added to an anhydrous ethanol solvent. It was then centrifuged at 8000 rpm for 10 min, washed with anhydrous ethanol three times, and vacuum dried at 60 $^\circ\text{C}$ for 24 h to obtain the final product (S-phosphor).

The phosphor obtained from the solvent thermal reaction was dispersed in 100 mL of anhydrous ethanol, stirred for 30 min, and then ultrasonicated for 30 min to separate the suspended and deposited portions. The suspended portion underwent solid-liquid separation after being centrifuged at 15,000 rpm for 5 min. The resulting nanophosphor was dried under vacuum at 60 $^\circ\text{C}$ for 24 h.

Commercial phosphors were sourced from Guangdong Yueke Xinfu New Material Co, Guangzhou, China. All reagents mentioned in this article were purchased from Aladdin Reagent (Shanghai, China) Co. All initial chemicals used in this paper were dried using molecular sieves (Shanghai Macklin Biochemical Technology Co., Shanghai, China).

The phase identification of the obtained samples was carried out with Ultima IV X-ray diffractometer. X-ray photoelectron spectroscopy (XPS) (Thermo Scientific K-Alpha, Waltham, MA, USA) was used for surface element analysis of phosphors. An Al Ka X-ray source with power of 150 W was used. Energy dispersive analysis (EDS) of phosphor was performed by JSM-7610Fplus. FE-SEM measurements were performed using FEI Verios 460 scanning electron microscopy. In order to improve the image quality, the samples were sputtered with high vacuum. TEM images were obtained using FEI Talos F200S, acceleration voltage of 200 KV. Selective area electron diffraction (SAED) and lattice fringe photography were performed using JEOL JEM-F200 HRTEM at 200 kV. Atomic Force microscope (AFM) images were obtained by Bruker Dimension Icon Atomic Force microscope. Atomic force microscopy (AFM) is a technique that involves fixing one end of a pair of microcantilevers, which are sensitive to weak forces. The tip of the other end was then scanned on the surface of the sample in order to obtain the topographical structure and roughness information of the sample surface with nanometer resolution. The size

distribution of the particles was analyzed using the laser size analyzer Mastersizer 3000. The excitation spectrum, emission spectrum, and afterglow attenuation curve were recorded by Hitachi F-7000 spectrophotometer, and 150 W xenon lamp was used as excitation source. The width of excitation and emission slit was 5 nm. When the sample was excited for 3 min, the excitation light of the sample was blocked, and the afterglow of the sample was measured. For temperature-dependent spectral measurements, the Edinburgh FLS980 was used.

3. Results and Discussion

3.1. Characterization and Optical Properties of S-Phosphor

As can be seen from Figure 1a, the monoclinic diffraction peaks of the reacted phosphor dominate in the XRD spectra, which were similar to those of the SAOED before the reaction. It indicates that the crystal structure of the phosphor was not destroyed after treatment. As shown in Figure 1b, the broad XPS spectra of the solvent-heat-treated phosphor in the range of 0~1200 eV showed the presence of Sr (3s, 3p, 3d), Al (2s, 2p), O1s, and C1s peaks in the spectra, which indicated that the product consisted of strontium, aluminum, and oxygen elements. The results of the XPS analyses indicated that the compositions of the reacted phosphors were essentially the same as those of the untreated bulk phosphor. EDX spectroscopy (Figure 1c) further confirmed the chemical composition of the products. The mass and atomic ratios of the elements of the untreated bulk phosphor and the reacted phosphor conform to the stoichiometric formula of SrAl_2O_4 . Figure 1f shows HRTEM images taken on the reacted phosphor. The spacing between neighboring lattice planes was 0.201 nm, which corresponds to the (-2 2 2) crystal planes of Joint Committee on Powder Diffraction Standards (JCPDS) standard card No. 34-0379.

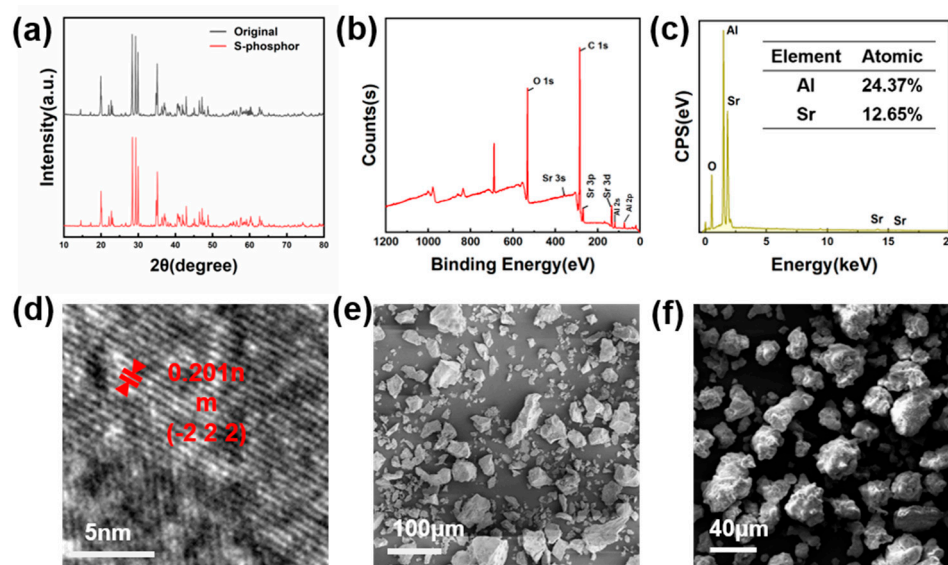


Figure 1. (a) X-ray diffraction (XRD) patterns of original phosphors and S-phosphor. (b) X-ray photoelectron spectroscopy (XPS) pattern of S-phosphor. (c) Energy dispersive analysis (EDS) pattern of S-phosphor. (d) Selective area electron diffraction (SAED) pattern of S-phosphor. (e) Scanning electron microscopy (SEM) image of original phosphors. (f) SEM image of S-phosphor.

As can be seen in Figure 1e,f, as well as Figure 2, the overall particle size of the phosphor was reduced from 42.3 μm to 23.6 μm after solvent heat treatment, and the change in particle size was obvious. Although the average size cannot be directly reduced to nanometer size or submicron size, the phosphor size in the submicron size range before and after the reaction was increased from 0.56% to 3.158% by volume. Compared with the untreated phosphor, most of the surface corners of the reacted phosphor became less obvious.

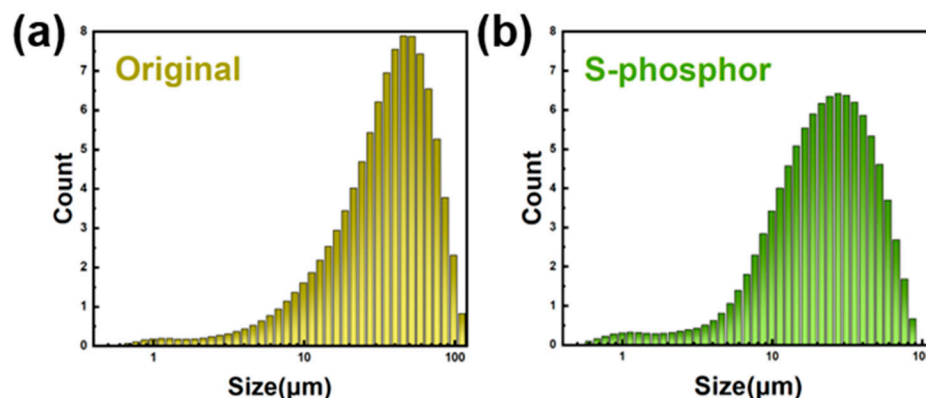


Figure 2. Size distribution of: (a) Original phosphor and (b) S-phosphor.

As can be seen in Figure 3, the excitation and emission spectra of the phosphor remain relatively stable in their positions before and after the reaction. The excitation spectrum consists mainly of excitation bands in the wavelength range of 300–450 nm, with a distinct peak at 360 nm and a shoulder peak at 420 nm. This indicates that the sample has a good excitation response to both UV and visible light. On the other hand, the emission spectrum shows a symmetrical and continuous broadband spectral pattern with the emission peak clearly located at 512 nm, and the emission intensity of S-phosphor remains at 91.39% of the original sample. This peak was mainly attributed to the radiative excitation process between the $4f^6 5d^1$ excited state and the $4f^7$ ground state of the Eu^{2+} ion [39]. In addition, the afterglow decay curves before and after the reaction show a similar trend, and the afterglow lifetime of S-phosphor was 94.98% of the original sample. This indicates that the luminescence center of the phosphor and its crystal structure were not significantly damaged after the dynamic solvent heat treatment.

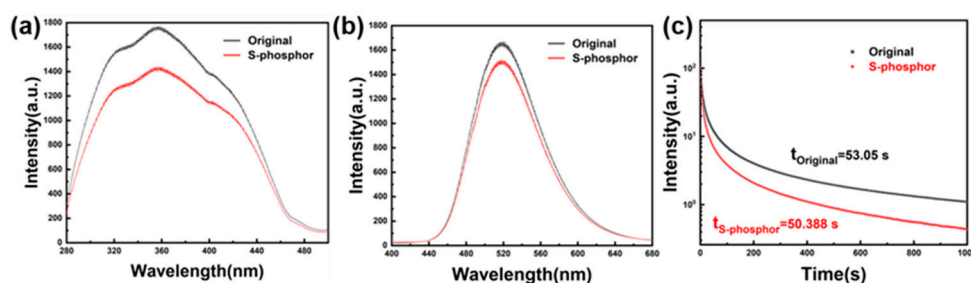


Figure 3. (a) Excitation spectra, (b) emission spectra, and (c) afterglow decay curves of original phosphors and S-phosphor.

In this work, we found that during the reaction process, cracks appeared in the phosphor blocks and “tore” at the cracks, thus splitting the large-particle block phosphor into multiple small-particle block phosphors. In the reaction kettle, we added a magnetic stirrer and stirred while reacting. The block phosphor was constantly subjected to pressure and solvent washing inside the kettle, and the block produced cracks during the reaction process. The surface of the untreated strontium aluminate luminescent material was relatively smooth, and no cracks appeared (Figure 4a). After 1 h of solvent heat treatment, the surface of the blocks started to become uneven, and cracks started to appear at the edges (Figure 4b). At 4 h of reaction, the cracks in the blocks became more pronounced (Figure 4c). When the reaction was carried out for 8 h, cracks appeared in most of the phosphor powder and even in most of the small particles of phosphor, and the number of cracks increased dramatically (Figure 4d). At 12 h (Figure 4e), the phosphor surface was covered by a large number of small irregular particles of phosphor, the powder was eroded significantly, the cracks turned into grooves, and the “tearing” phenomenon began to appear. At 24 h of reaction (Figure 4f), the number of cracks in the powder was significantly reduced and was

not obvious; the powder became uneven, and rough “pits” appeared. Scanning electron microscopy (SEM) analysis of the “cracked” parts of the powder (Figure 4g,h) revealed that the fracture was uneven, the surface was rough, and irregular grooves appeared, similar to the phenomenon of wall cracked. In addition, a large number of submicron-sized phosphors were agglomerated at the cracked area (Figure 4i).

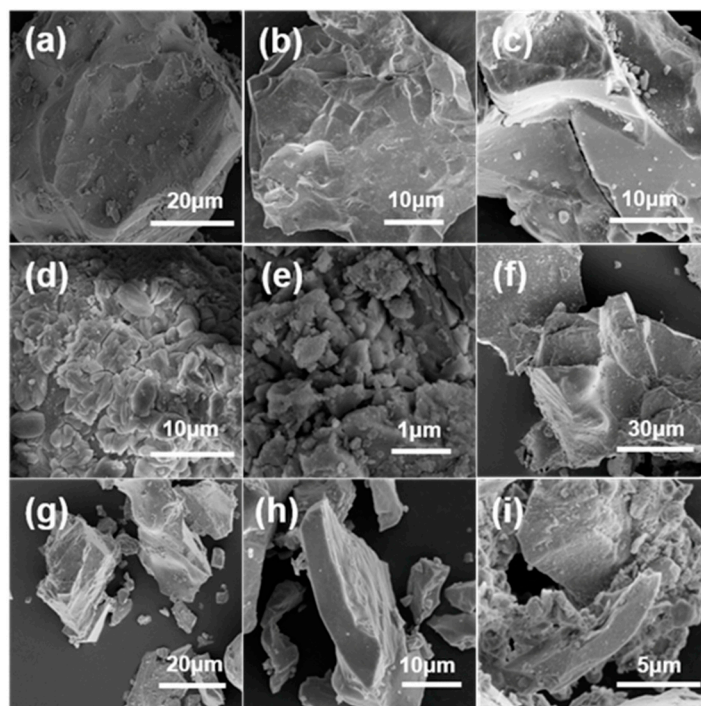


Figure 4. Scanning electron microscopy (SEM) images of cracks appearing during the reaction process. (a) Untreated commercial phosphor; (b) 1 h; (c) 4 h; (d) 8 h; (e) 12 h; (f) 24 h; (g–i) block tearing surface.

Therefore, this work proposes a mechanism for the fragmentation of phosphor powder (Figure 5); with the beginning of the solvothermal reaction, part of the large-size phosphor was gradually eroded and peeled off from the smooth surface of the powder by the influence of high-temperature and high-pressure conditions and stirring in the reaction kettle, and the corners of the powder diamonds also gradually became smooth. As the reaction proceeded, the surface of the powder became rougher and rougher, and cracks began to appear, gradually cracking. At the same time, some of the stripped small-sized phosphor was attached to the surface of the block. As the reaction continued, the large-sized powder was “torn” into small-sized particles, which ultimately led to a reduction in the overall particle size of the phosphor.

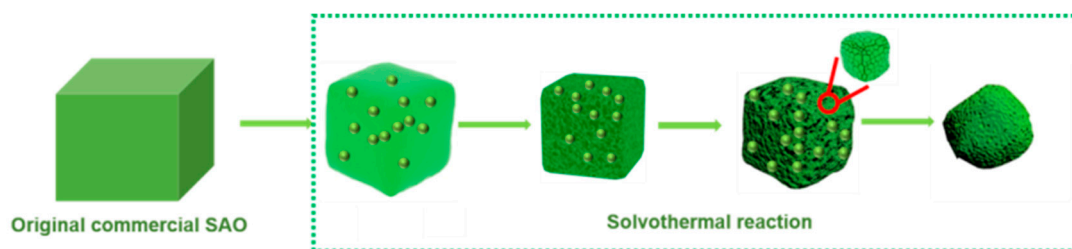


Figure 5. Crushing mechanism of block phosphor.

In order to explore the applicability of this solvent heating method to the same phosphor with different particle sizes, SAOED with 6.32 μm , 24.6 μm , and 61.2 μm particle sizes were also subjected to cyclohexane solvent heating in this work. The emission spectra

(Figure 6a) show that the optical properties of SAOED with different particle sizes were weakened to a certain extent after solvent heat treatment, which corresponds to the reduction of the overall particle size from 6.32 μm to 4.86 μm (Figure 6b), 24.6 μm to 12.6 μm (Figure 6c), and 61.2 μm to 45.8 μm (Figure 6d). The commercial $\text{Sr}_4\text{Al}_{14}\text{O}_{25}$ phosphor with 20 μm particle size and the commercial $\text{Sr}_2\text{MgSi}_2\text{O}_7$ phosphor with 20 μm particle size were also taken to explore the universality of this solvent-heating method for different phosphors with the same particle size. It can be found that, after solvent-heating treatment, the optical properties of the two were weakened compared with those of the commercial phosphors before the treatment (Figure 6e,f), and the changes in the particle size were consistent with the results of the previous experiments. The changes in particle size were also consistent with the previous experimental results, and the overall average particle size after the solvent thermal reaction was reduced compared with that of the untreated commercial phosphor. Moreover, the volume percentage of submicron size increased compared with that before the reaction (Figure 6g,h). Therefore, it can be seen that the solvothermal method in this work is universal.

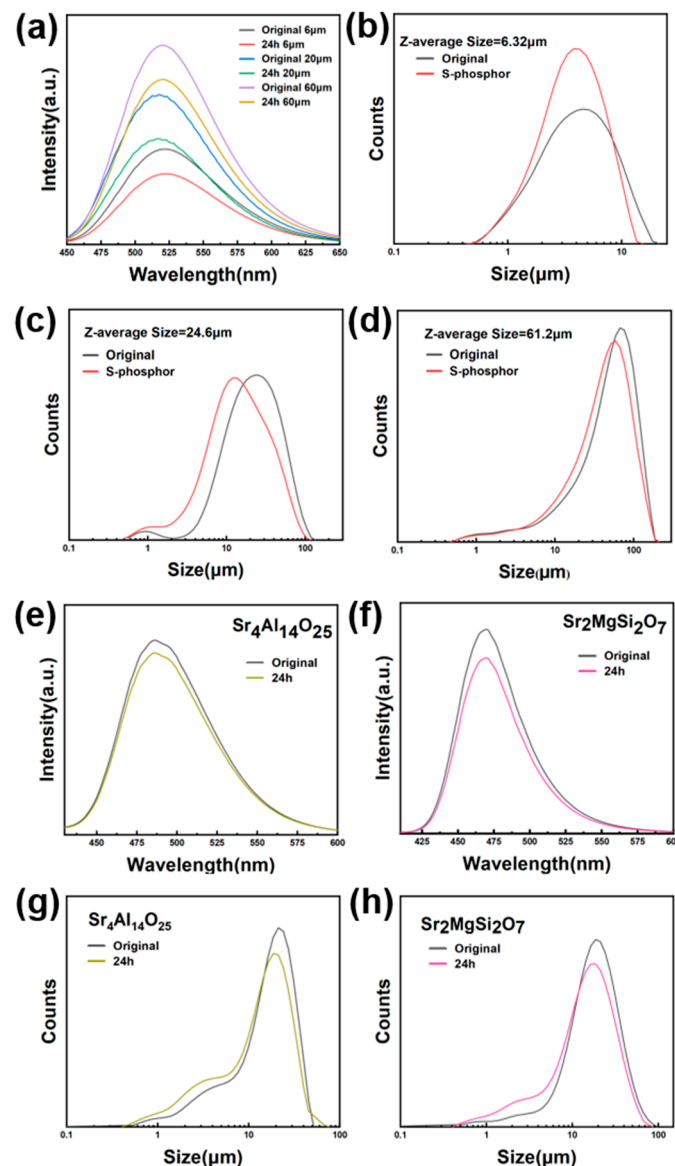


Figure 6. Before and after reaction. (a) Emission spectra of $\text{SrAl}_2\text{O}_4:\text{Eu}^{2+}$, Dy^{3+} phosphors (SAOED) with different particle sizes. (b–d) Size distribution of SAOED with different particle sizes. Emission spectra of (e) $\text{Sr}_4\text{Al}_{14}\text{O}_{25}$ and (f) $\text{Sr}_2\text{MgSi}_2\text{O}_7$. Size distribution of (g) $\text{Sr}_4\text{Al}_{14}\text{O}_{25}$ and (h) $\text{Sr}_2\text{MgSi}_2\text{O}_7$.

As the reaction proceeded, the surface of the bulk phosphor was continuously washed by the solvent under high temperature, high humidity, and high pressure, in which the surface morphology of the bulk changed continuously during the reaction, so the powders were analyzed by field emission scanning electron microscopy (FESEM) after the solvent heat treatment at different times. It can be seen that the surface of the untreated strontium aluminate luminescent material was relatively smooth (Figure 7a). At 4 h of solvent heat treatment, the surface of the block started to become rough and uneven, and a number of small-sized (<2 μm) phosphor particles were attached to the surface (Figure 7b). At 12 h of treatment, grooves different from the previously discussed tearing surface appeared, and the direction of the grooves showed regularity, while the corners of the blocks began to become less obvious (Figure 7c). When treated for 18 h, part of the needle-like morphology phosphor began to adhere to the surface of the grooves of the large-grained bulk phosphor (Figure 7d). Further increasing the treatment time to 24 h (Figure 7e), it was found that the surface of the large-particle chunks had basically been covered by the small-sized and needle-shaped phosphors. As the experiment proceeded to 48 h (Figure 7f), the needle phosphors appeared to agglomerate and formed uniformly covered cluster needle structures on the block phosphor surface. It was found that the surface of the bulk phosphor will be eroded by the solvent, and with the increase of the experimental time, in the middle and late stages of the reaction, the surface of the block will gradually generate nano-sized special features and the present experiment mainly generates needle-like special features and some flaky special features.

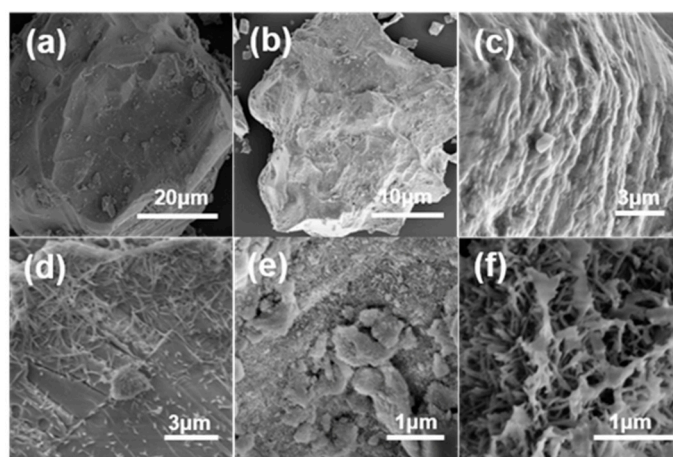


Figure 7. Scanning electron microscopy (SEM) images of surface morphology change of bulk phosphor after solvent thermal reaction with different reaction times. (a) Untreated commercial phosphor; (b) 4 h; (c) 12 h; (d) 18 h; (e) 24 h; (f) 48 h.

3.2. Characterization and Optical Properties of Nanophosphor

In order to separate these small-sized and nano-sized phosphors from the surface of the block, after solvent-thermal reaction, the phosphors were further processed by ultrasonication and centrifugation. The scanning electron microscope images showed that the small-sized phosphors were relatively uniform in size, numerous, and with a greatly reduced particle size (Figure 8a). The powders were in the form of clusters, similar to coral structures, and were all similar to coral structures (Figure 8b,c). The average length of the needle-like structure on the coral structure was about 568 nm, and the average diameter was about 63 nm, while the average length of the lamellar structure was about 300 nm (Figure 8d). At the same time, the length and diameter of the separated and extracted needle phosphors were less than 100 nm, and the morphology was approximately the same (Figure 8e). This indicates that the uniform size of the nanofluorescent needles can be extracted by solvent heat. The surface of the bulk phosphor after the isolation of the nanospecific morphology was rough and covered with grooves (Figure 8f), which was

similar to the morphology at 12 h of reaction (Figure 7c), which can be added to prove that the small-sized special morphology was reattached and agglomerated on the surface of the bulk powder in the middle and late stages of the reaction.

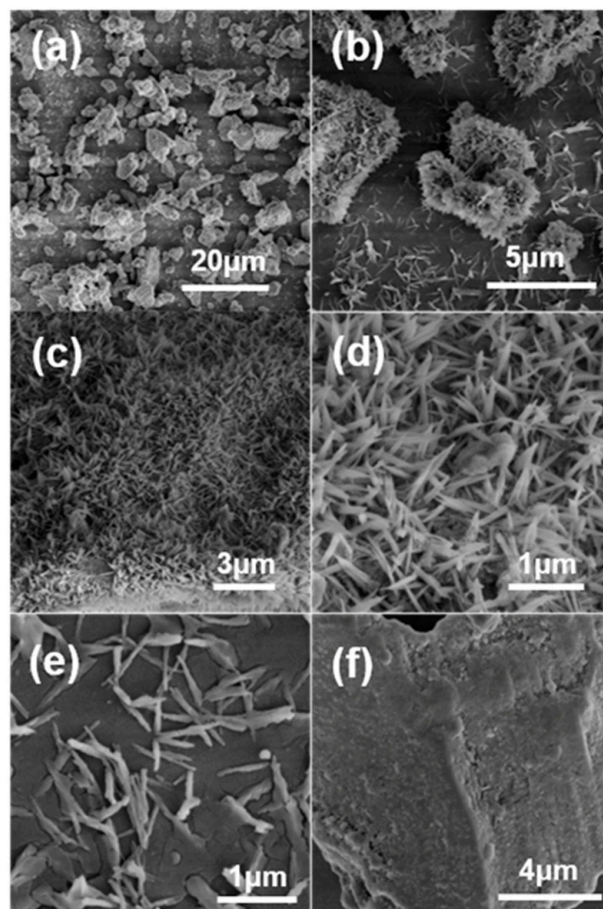


Figure 8. Scanning electron microscopy (SEM) image of phosphor after ultrasonic dispersion. (a,b) Overall morphology of block phosphor. (c,d) Surface morphology of block phosphor. (e) Needle phosphor extracted by ultrasound. (f) Block phosphor after extraction of needle phosphor.

During the previous experiments, after the operations of ultrasonication and centrifugation, the submicron-size and nanosize phosphors in the products were extracted, which had needle-like morphology with some flake-like morphology. In the XRD spectrum (Figure 9a), the monoclinic diffraction peaks of the small-sized phosphors were dominant, similar to those of the commercial SAOED before the reaction. It indicates that the crystal structure of the nanophosphor was not destroyed after treatment, but the summit appears broadened, which was due to the small size effect of the particles. The EDS spectra (see Figure 9b) further confirmed the chemical composition of the final products. The mass and atomic ratios of the elements of the untreated bulk and nanopowder phosphors conform to the stoichiometric formula of SrAl_2O_4 .

Wide XPS spectra showed (Figure 9c) the presence of Sr (3s, 3p, 3d), Al (2s, 2p), O1s, and C1s peaks in the spectra, suggesting that the extracted product consisted of the elements strontium, aluminum, and oxygen. The results of the XPS analyses indicated that the composition of the nanophosphors was essentially the same as that of the untreated commercial bulk phosphor.

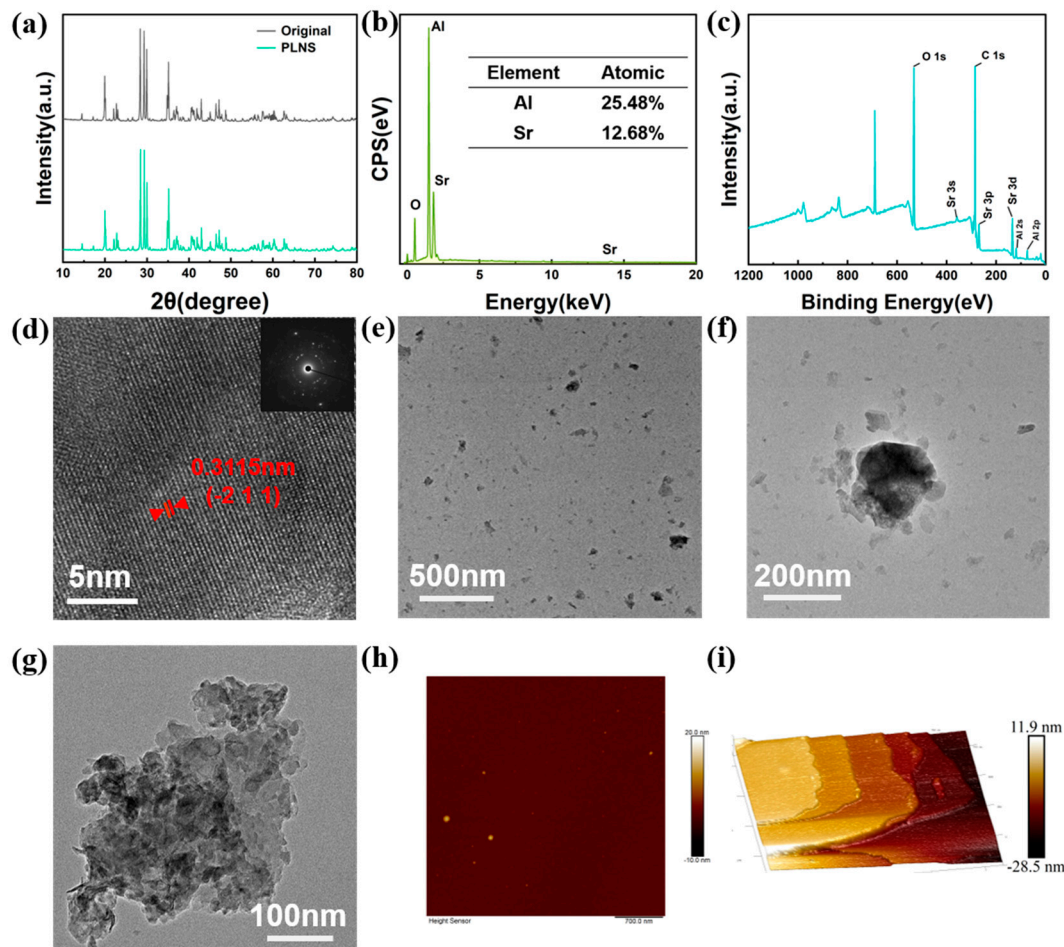


Figure 9. (a) X-ray diffraction (XRD) spectra of the nanophosphor; (b) energy dispersive analysis (EDS) spectra of the nanophosphor; (c) X-ray photoelectron spectroscopy (XPS) spectra of the nanophosphor; (d) lattice fringes of the nanophosphor (insets are diffractograms); (e–g) HRTEM images of the nanophosphor; (h,i) atomic force microscopy (AFM) images of the nanophosphor.

HRTEM images taken of the nanofluorescent powders were adjacent to their lattice plane spacing of 0.3115 nm, corresponding to the $(-2\ 1\ 1)$ crystal plane of JCPDS standard card No. 34-0379 (Figure 9d). Transmission electron microscopy (Figure 9e–g) and AFM analysis (Figure 9h,i) observations showed that the product nanopins or nanosheets (PLNSs) were very thin, and the nanopins were well dispersed, whereas most of the PLNSs were in the form of irregular flakes and prone to agglomeration, with an average particle size of 86 nm and an average thickness of about 15 nm.

To demonstrate the feasibility of preparing nano-sized phosphor through this experiment, we extracted the nano phosphor from the original commercial bulk phosphor and compared its weight with that of the phosphor obtained in this experiment. The experiment demonstrates that the weight of the nano phosphor in the pristine bulk phosphor was 0.2675 g, while the weight of the nano phosphor obtained by solvent heat treatment was 0.8314 g. This confirms the successful preparation of the nano phosphor with a yield of 5.64%.

Temperature-dependent emission spectra were carried out for the product nanofluorescent powder at 45 K intervals between 100 and 460 K with xenon excitation (Figure 10a). In the emission spectrum, two bands were observed at 440 to 525 nm. This is due to the presence of two sites available for Sr^{2+} ions in monoclinic crystalline SAOED, and both sites occur in the same number in the lattice [40]. The emission intensity at shorter wavelengths is slightly lower due to energy transfer. At room temperature, the emission at 445 nm

was quenched, and only the longer wavelength emission was observed. However, in the present work, the emission spectra show a blue shift with increasing temperature. The reason for this may be that at higher temperatures, more electrons were populated on the high-energy excited state subenergy levels, but the non-radiative leaps at the intersection of excited and ground states in the configuration coordinate diagram were reduced. As a result, the intensity of the high-energy emission peaks increased, and the intensity of the low-energy emission peaks decreased. Also, due to the convolution of the peaks, the blue-shifted behavior was observed with increasing temperature.

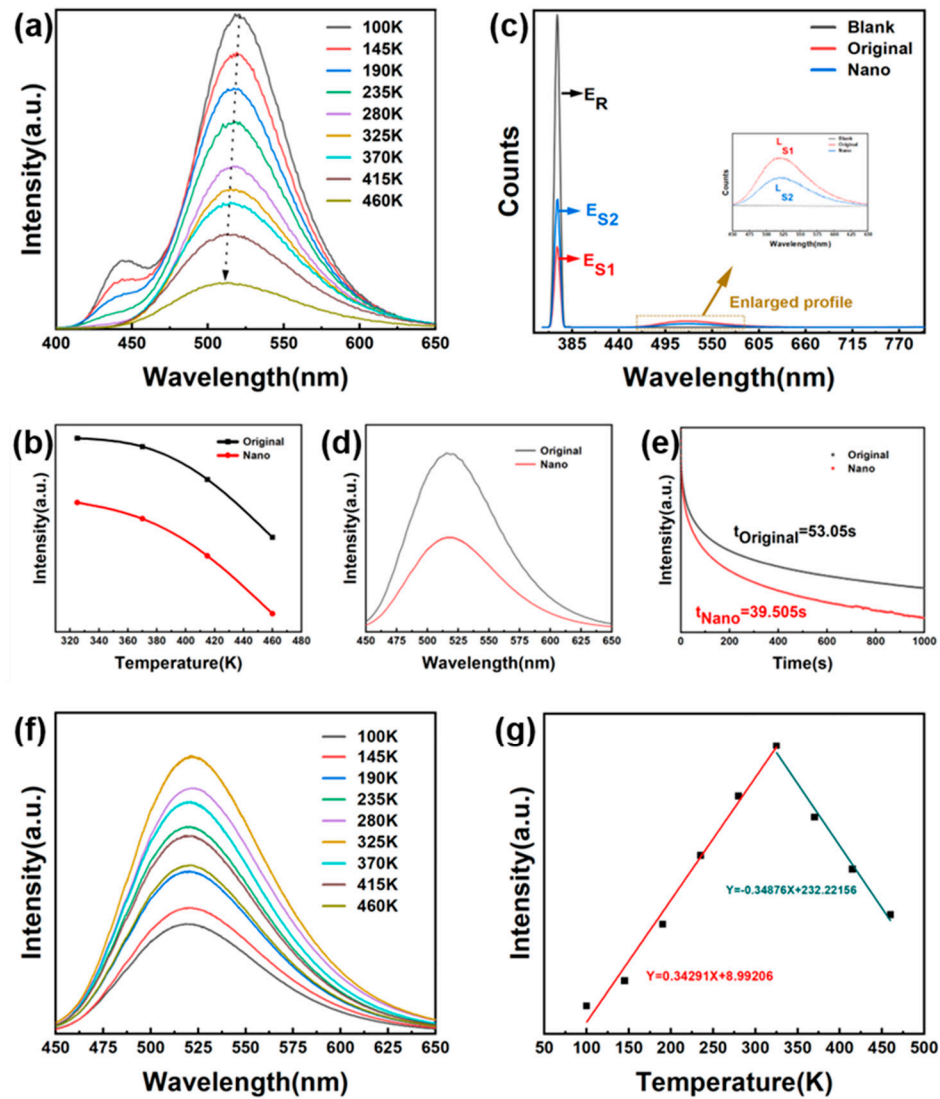


Figure 10. (a) Variable temperature emission spectrum. (b) Temperature-dependent emission intensity in the range of 325–460 K. (c) Quantum efficiency plot. (d) Emission spectrum. (e) Room temperature afterglow decay curve. (f) Variable temperature phosphorescence emission spectroscopy. (g) Afterglow intensity at different temperatures.

Due to the electron–phonon interaction between the ground and excited states of the luminescent center at high temperatures, the emission intensity decreases with increasing temperature. It was assumed that the non-emissivity k_{nr} can be expressed as [41]

$$K_{nr} = A \exp(-\Delta E/kT) \tag{1}$$

where A is a constant, k is the Boltzmann constant, and ΔE is the activation energy of the thermal quenching process. Therefore, the emission intensity decreases as the probability

of non-radiative jump increases with increasing temperature. From Equation (1), the lower the value of ΔE , the faster the non-radiative rate at a given temperature [42]. In addition, the Arrhenius equation can be used to characterize the temperature quenching of the study [43].

$$I(T) = I_0 / [1 + C \exp(-\Delta E/kT)] \quad (2)$$

where I_0 and $I(T)$ are the initial intensity and the intensity at a given temperature T , respectively, and C is a constant. Comparing the emission intensities (Figure 10b) with temperature in the range of 325 to 460 K, the ΔE of commercial SAOED and nanophosphor were obtained as 0.067 and 0.061 eV, respectively, and there was no doubt that the activation energies of unreacted commercial SAOED were higher than that of the nanophosphor, which suggests that the latter's thermal stability has been improved while being more sensitive to thermal effects.

In order to visualize the optical strength of the two, the phosphor quantum efficiency test was performed by exciting the phosphor at 370 nm (Figure 10c). The quantum efficiency is the ratio of the number of photons produced per second by the phosphor to the number of incident quanta at a particular wavelength. The quantum efficiency can be calculated for the resulting nanosheets by the following equation [44]:

$$\eta = \frac{\varepsilon}{\alpha} = \frac{\int L_S}{\int E_R - \int E_S} \quad (3)$$

In the formula, ε is the number of photons emitted by the sample; α is the number of photons absorbed by the sample; L_S is the emission spectrum of the sample; E_S is the excitation spectrum of the standard light source, and E_R is the excitation spectrum of the sample without the sample in the integrating sphere. After calculation, the absorption efficiency of nanosheet strontium aluminate is 23.40%, while the absorption efficiency of commercial strontium aluminate luminous powder is 31.86%. The quantum efficiency of nanosheet strontium aluminate luminescent powder was lower than that of commercialized bulk strontium aluminate luminescent powder, and the level of quantum efficiency essentially reflects the luminescence intensity of luminescent powder; therefore, the luminescence intensity of nanosheet luminescent powder was also slightly lower than that of commercialized strontium aluminate luminescent material. The results were shown to correspond to the intensity of the emission peaks of both in the fluorescence spectrogram (Figure 10d).

Afterglow performance is an important indicator of the optical properties of phosphors, and in this work, it was observed that the afterglow decay curves of the samples contained two processes (Figure 10e): a fast-decay phase and a slow-decay phase. The fast decay stage is a stage in which the electron inventory inside the luminescent center Eu^{2+} is short, and thus, a rapid decrease in the afterglow intensity occurs; the slow decay stage was caused by the Dy^{3+} ions, which provide a deeper trap energy level in the SAOED, and the electrons were trapped in the process of irradiation of excitation source, and after the excitation source was cut off, the trapped electrons were slowly released, slowing down the rate of decrease in the afterglow intensity of the sample.

The afterglow decay curves of SAOED bulk luminescent materials, as well as nanophosphors, were fitted using Equation (4):

$$Y = Y_0 + A_1 \exp(-t/t_1) + A_2 \exp(-t/t_2) \quad (4)$$

where Y is the photoluminescence intensity; Y_0 , A_1 , A_2 are the material correlation constants; t is the desired afterglow time; and t_1 , t_2 are the fitting parameters related to the phosphor decay rate, which correspond to the two decay processes. From the results, it can be seen that the fluorescence brightness of the nano phosphor was 53.06% of the original sample (Figure 10d), and the afterglow lifetime was 74.47% of the original sample, but it was still better compared with the afterglow performance of other nano-sized phosphors obtained by the top-down method [25,45].

Similarly, we studied the variation of afterglow intensity with temperature by ramping up from 100 K to 460 K at 45 K intervals (Figure 10f). When the temperature was less than 150 K, the afterglow intensity was weak due to the lower temperature and weaker thermal perturbation; subsequently, when the temperature increases to 325 K, the process of trapping and releasing electrons becomes more and more active with the increase of temperature, and thus the afterglow intensity shows a linear increase in this temperature band; when 320 K–460 K, the afterglow intensity shows a linear decay relationship (Figure 10g), which was due to the thermal disturbance caused by the ambient temperature. Induced thermal disturbances were too strong, and internal carrier storage in different traps became difficult. In this case, electrons escape or are lost, and thus, the emission intensity of the afterglow becomes weaker. In addition, the nanosheet afterglow intensity varies linearly with the ambient temperature, which can be applied to fiber optic sensing materials.

3.3. Nanophosphor Fingerprint Imaging Applications

In this work, the experimenter pressed the finger on A4 paper (Figure 11a) and a door handle (Figure 11d), and it was difficult to see the fingerprint details with the naked eye in both cases. The nanophosphor obtained by the solvent heat treatment was applied to the pressed area, and the complete fingerprint image could be seen after turning on (Figure 11b,e) and off (Figure 11c,f) the UV light, and the clean ridges and edges could be observed by the naked eye, and some unique texture details (core, bifurcation, termination, pores, and islands) could be well observed after magnification of some areas of the fingerprint photo. It was demonstrated that the nanophosphor obtained in this work shows great potential for practical applications in the visualization and detection of fast fingerprint identification.

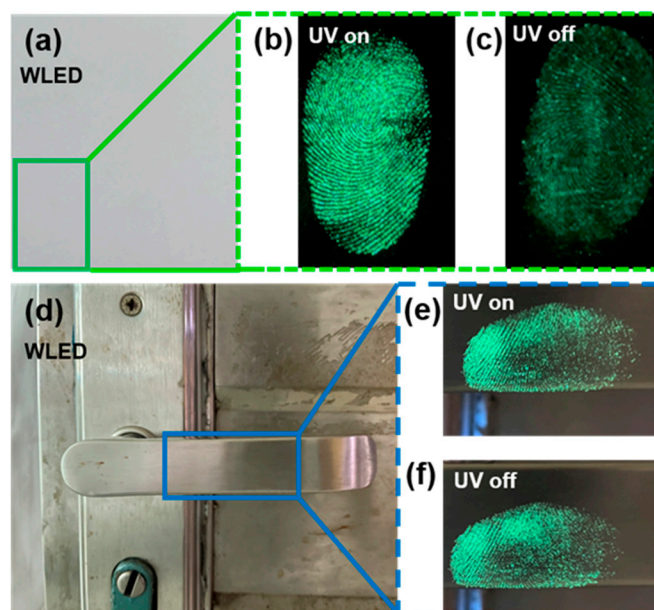


Figure 11. Fingerprint imaging applications.

4. Conclusions

In this study, we successfully reduced the average particle size of commercialized phosphor from 42.3 μm to 23.6 μm without compromising its optical properties. The fluorescence intensity was maintained at 91.39% of the original sample using the dynamic solvent–thermal method with low-polar or non-polar solvents to treat micrometer-sized commercialized phosphors. We also observed the change in particle size without affecting its optical properties. The method was applicable to most inorganic long afterglow luminescent materials. We propose the related mechanism for the first time.

Nanophosphors with good afterglow properties were prepared using a one-step solvothermal method. These nanophosphors have great potential for practical applications in visualization and rapid fingerprinting. The average diameter and thickness of the nanophosphors were 85 nm and 16 nm, respectively. The quantum efficiency of the nanophosphors was 74.46% of that of the original sample. The high temperature and high pressure generated by the direct thermal treatment of solvents and stirring ensure their great potential for biological applications. The relationship between the photoluminescence and afterglow emission intensity of the material was linear with respect to ambient temperature, indicating potential application in temperature-sensing materials.

Author Contributions: Conceptualization, R.L. and Y.L.; methodology, R.L., X.L. and W.L.; software, R.L.; validation, R.L., X.L. and Y.L.; formal analysis, R.L.; investigation, R.L. and W.L.; resources, R.L. and Y.L.; data curation, R.L. and X.L.; writing—original draft preparation, R.L. and Y.L.; writing—review and editing, X.L. and Y.L.; visualization, R.L.; funding acquisition, Y.L. All authors have read and agreed to the published version of the manuscript.

Funding: This research was funded by the National Natural Science Foundation of China (12174119).

Institutional Review Board Statement: Not applicable.

Informed Consent Statement: Not applicable.

Data Availability Statement: All data generated or analyzed during this study are included in this article.

Conflicts of Interest: The authors declare no conflicts of interest.

References

1. Huang, K.; Le, N.; Wang, J.S.; Huang, L.; Zeng, L.; Xu, W.C.; Li, Z.J.; Li, Y.; Han, G. Designing Next Generation of Persistent Luminescence: Recent Advances in Uniform Persistent Luminescence Nanoparticles. *Adv. Mater.* **2022**, *34*, 2107962. [[CrossRef](#)]
2. Pan, Z.W.; Lu, Y.Y.; Liu, F. Sunlight-activated long-persistent luminescence in the near-infrared from Cr³⁺-doped zinc gallogermanates. *Nat. Mater.* **2012**, *11*, 58–63. [[CrossRef](#)]
3. Yang, X.; Waterhouse, G.I.N.; Lu, S.Y.; Yu, J.H. Recent advances in the design of afterglow materials: Mechanisms, structural regulation strategies and applications. *Chem. Soc. Rev.* **2023**, *52*, 8005–8058. [[CrossRef](#)]
4. Li, Y.; Gecevicius, M.; Qiu, J.R. Long persistent phosphors—from fundamentals to applications. *Chem. Soc. Rev.* **2016**, *45*, 2090–2136. [[CrossRef](#)]
5. Li, Y.J.; Teng, X.C.; Wang, Y.J.; Yang, C.R.; Yan, X.P.; Li, J.H. Neutrophil Delivered Hollow Titania Covered Persistent Luminescent Nanosensitizer for Ultrasound Augmented Chemo/Immuno Glioblastoma Therapy. *Adv. Sci.* **2021**, *8*, e2004381. [[CrossRef](#)] [[PubMed](#)]
6. Shu, G.; Zhu, W.; Jiang, Y.Z.; Li, X.W.; Pan, J.B.; Zhang, X.N.; Zhang, X.J.; Sun, S.K. Persistent Luminescence Immune Hydrogel for Photodynamic-Immunotherapy of Tumors In Vivo. *Adv. Funct. Mater.* **2021**, *31*, 2104472. [[CrossRef](#)]
7. Feng, S.W.; Ma, Y.J.; Wang, S.Q.; Gao, S.S.; Huang, Q.Q.; Zhen, H.Y.; Yan, D.P.; Ling, Q.D.; Lin, Z.H. Light/Force-Sensitive 0D Lead-Free Perovskites: From Highly Efficient Blue Afterglow to White Phosphorescence with Near-Unity Quantum Efficiency. *Angew. Chem. Int. Ed.* **2022**, *61*, e202116511. [[CrossRef](#)]
8. Huang, Q.Q.; Gao, H.Q.; Yang, S.M.; Ding, D.; Lin, Z.H.; Ling, Q.D. Ultrastable and colorful afterglow from organic luminophores in amorphous nanocomposites: Advanced anti-counterfeiting and in vivo imaging application. *Nano Res.* **2020**, *13*, 1035–1043. [[CrossRef](#)]
9. Jin, X.Y.; Wang, Z.Y.; Xu, H.Y.; Jia, M.C.; Fu, Z.L. Combining time-evolving multicolor luminescence with intense afterglow of Na₂CaGe₂O₆: Tb³⁺/Tb³⁺, Yb³⁺ phosphors for dynamic anticounterfeiting. *Mater. Today Chem.* **2022**, *24*, 100771. [[CrossRef](#)]
10. Fatemina, S.M.A.; Mao, Z.; Xu, S.D.; Yang, Z.Y.; Chi, Z.G.; Liu, B. Organic Nanocrystals with Bright Red Persistent Room-Temperature Phosphorescence for Biological Applications. *Angew. Chem. Int. Ed.* **2017**, *56*, 12160–12164. [[CrossRef](#)]
11. Wang, Y.K.; Chen, D.R.; Zhuang, Y.X.; Chen, W.J.; Long, H.Y.; Chen, H.M.; Xie, R.J. NaMgF₃:Tb³⁺@NaMgF₃ Nanoparticles Containing Deep Traps for Optical Information Storage. *Adv. Opt. Mater.* **2021**, *9*, 2100624. [[CrossRef](#)]
12. Zheng, Y.H.; Wei, H.P.; Liang, P.; Xu, X.K.; Zhang, X.C.; Li, H.H.; Zhang, C.L.; Hu, C.F.; Zhang, X.J.; Lei, B.F.; et al. Near-Infrared-Excited Multicolor Afterglow in Carbon Dots-Based Room-Temperature Afterglow Materials. *Angew. Chem. Int. Ed.* **2021**, *60*, 22253–22259. [[CrossRef](#)] [[PubMed](#)]
13. Kang, F.W.; Sun, G.H.; Boutinaud, P.; Wu, H.Y.; Ma, F.X.; Lu, J.; Gan, J.L.; Bian, H.D.; Gao, F.; Xiao, S.S. working Recent advances and prospects of persistent luminescent materials as inner secondary self-luminous light source for photocatalytic applications. *Chem. Eng. J.* **2021**, *403*, 126099. [[CrossRef](#)]

14. Pei, P.; Chen, Y.; Sun, C.; Fan, Y.; Yang, Y.; Liu, X.; Lu, L.; Zhao, M.; Zhang, H.; Zhao, D.; et al. X-ray-activated persistent luminescence nanomaterials for NIR-II imaging. *Nat. Nanotechnol.* **2021**, *16*, 1011–1018. [[CrossRef](#)] [[PubMed](#)]
15. Han, C.M.; Du, R.M.; Xu, H.; Han, S.Y.; Ma, P.; Bian, J.K.; Duan, C.B.; Wei, Y.; Sun, M.Z.; Liu, X.G.; et al. Ladder-like energy-relaying exciplex enables 100% internal quantum efficiency of white TADF-based diodes in a single emissive layer. *Nat. Commun.* **2021**, *12*, 3640. [[CrossRef](#)] [[PubMed](#)]
16. Jeon, S.O.; Lee, K.H.; Kim, J.S.; Ihn, S.-G.; Chung, Y.S.; Kim, J.W.; Lee, H.; Kim, S.; Choi, H.; Lee, J.Y. High-efficiency, long-lifetime deep-blue organic light-emitting diodes. *Nat. Photonics* **2021**, *15*, 208–215. [[CrossRef](#)]
17. Liu, X.Y.; Wu, W.J.; Cui, D.X.; Chen, X.Y.; Li, W.W. Functional Micro-/Nanomaterials for Multiplexed Biodetection. *Adv. Mater.* **2021**, *33*, 2004734. [[CrossRef](#)] [[PubMed](#)]
18. Sun, X.; Song, L.; Liu, N.A.; Shi, J.P.; Zhang, Y. Chromium-Doped Zinc Gallate Near-Infrared Persistent Luminescence Nanoparticles in Autofluorescence-Free Biosensing and Bioimaging: A Review. *ACS Appl. Nano Mater.* **2021**, *4*, 6497–6514. [[CrossRef](#)]
19. Yang, Y.L.; Yang, X.C.; Yuan, J.Y.; Li, T.; Fan, Y.T.; Wang, L.; Deng, Z.; Li, Q.L.; Wan, D.Y.; Zhao, J.T.; et al. Time-Resolved Bright Red to Cyan Color Tunable Mechanoluminescence from CaZnOS: Bi³⁺, Mn²⁺ for Anti-Counterfeiting Device and Stress Sensor. *Adv. Opt. Mater.* **2021**, *9*, 2100668. [[CrossRef](#)]
20. Zhang, K.Y.; Yu, Q.; Wei, H.; Liu, S.; Zhao, Q.; Huang, W. Long-Lived Emissive Probes for Time-Resolved Photoluminescence Bioimaging and Biosensing. *Chem. Rev.* **2018**, *118*, 1770–1839. [[CrossRef](#)]
21. Dang, P.P.; Wei, Y.; Liu, D.J.; Li, G.G.; Lin, J. Recent Advances in Chromium-Doped Near-Infrared Luminescent Materials: Fundamentals, Optimization Strategies, and Applications. *Adv. Opt. Mater.* **2023**, *11*, 2201739. [[CrossRef](#)]
22. Kumar, A.; Crista, D.M.A.; Núñez-Montenegro, A.; da Silva, J.; Verma, S.K. Annealing-assisted optimization for persistency of afterglow of SrAl₂O₄:Eu²⁺/Dy³⁺ microparticles for forensic detection. *Rsc Adv.* **2023**, *13*, 28676–28685. [[CrossRef](#)] [[PubMed](#)]
23. Lee, C.M.; Liu, Y.H.; Hulme, B.; Chang, L.Y.; Ke, S.W.; Wang, E.R.; Wu, Y.H.; Lin, B.H.; Jiang, Y.Y.; Liu, L.J. ZnGa₂O₄:Cr³⁺@Calcium Phosphate Nanocomposite with Near-Infrared Persistent Luminescence and High Stability. *ChemPhotoChem* **2023**, *7*, e202300143. [[CrossRef](#)]
24. Rojas-Hernandez, R.E.; Rubio-Marcos, F.; Rodriguez, M.A.; Fernandez, J.F. Long lasting phosphors: SrAl₂O₄:Eu, Dy as the most studied material. *Renew. Sustain. Energy Rev.* **2018**, *81*, 2759–2770. [[CrossRef](#)]
25. Zhang, Q.; Wang, X.Q.; Wang, C.; Xiong, X.B.; Wang, Y.Q. Low-temperature and short-time preparation of short rod-like Zn₂GeO₄:Mn²⁺ luminescent nanoparticles. *J. Mater. Sci. Mater. Electron.* **2023**, *34*, 1477. [[CrossRef](#)]
26. Abdu, M.T.; Khattab, T.A.; Abdelrahman, M.S. Development of Photoluminescent and Photochromic Polyester Nanocomposite Reinforced with Electrospun Glass Nanofibers. *Polymers* **2023**, *15*, 761. [[CrossRef](#)] [[PubMed](#)]
27. Alam, P.; Cheung, T.S.; Leung, N.L.C.; Zhang, J.Y.; Guo, J.; Du, L.L.; Kwok, R.T.K.; Lam, J.W.Y.; Zeng, Z.B.; Phillips, D.L.; et al. Organic Long-Persistent Luminescence from a Single-Component Aggregate. *J. Am. Chem. Soc.* **2022**, *144*, 3050–3062. [[CrossRef](#)]
28. Vaidyanathan, S. Recent progress on lanthanide-based long persistent phosphors: An overview. *J. Mater. Chem. C* **2023**, *11*, 8649–8687. [[CrossRef](#)]
29. Wei, G.H.; Li, P.L.; Li, R.; Wang, Y.; He, S.X.; Li, J.H.; Shi, Y.W.; Suo, H.; Yang, Y.B.; Wang, Z.J. How to Achieve Excellent Luminescence Properties of Cr Ion-Doped Near-Infrared Phosphors. *Adv. Opt. Mater.* **2023**, *11*, 2301794. [[CrossRef](#)]
30. Yang, X.Y.; Tang, B.M.; Cao, X.J. The roles of dopant concentration and defect states in the optical properties of Sr₂MgSi₂O₇:Eu²⁺, Dy³⁺. *J. Alloys Compd.* **2023**, *949*, 169841. [[CrossRef](#)]
31. Matsuzawa, T.; Aoki, Y.; Takeuchi, N.; Murayama, Y. A New Long Phosphorescent Phosphor with High Brightness, SrAl₂O₄:Eu²⁺, Dy³⁺. *J. Electrochem. Soc.* **1996**, *143*, 2670. [[CrossRef](#)]
32. Gao, P.; Wang, J.G.; Wu, J.; Xu, Q.Q.; Yang, L.X.; Liu, Q.X.; Qi, Y.S.; Li, Z.J. Preparation of SrAl₂O₄:Eu²⁺, Dy³⁺ Powder by Combustion Method and Application in Anticounterfeiting. *Coatings* **2023**, *13*, 808. [[CrossRef](#)]
33. Gong, J.S.; Dai, W.B.; Luo, J.; Nie, K.; Xu, M. Insights into structure, local site symmetry, and energy transfer for regulating luminescent properties of SrLaLiTeO₆: Dy/Eu and its application in wLEDs. *Ceram. Int.* **2023**, *49*, 31024–31034. [[CrossRef](#)]
34. Huang, Z.F.; Chen, B.; Ren, B.Y.; Tu, D.; Wang, Z.F.; Wang, C.F.; Zheng, Y.T.; Li, X.; Wang, D.; Ren, Z.B.; et al. Smart Mechanoluminescent Phosphors: A Review of Strontium-Aluminate-Based Materials, Properties, and Their Advanced Application Technologies. *Adv. Sci.* **2023**, *10*, 2204925. [[CrossRef](#)] [[PubMed](#)]
35. Leimane, M.; Krizmane, K.; Bite, I.; Grube, J.; Vitola, V. Sol-Gel Synthesis of Translucent and Persistent Luminescent SiO₂@SrAl₂O₄ Eu, Dy, B Materials. *Materials* **2023**, *16*, 4416. [[CrossRef](#)] [[PubMed](#)]
36. Luo, J.; Ren, B.; Zhang, X.; Zhu, M.; Liang, T.; Huang, Z.; Zheng, Y.; Li, X.; Li, J.; Zheng, Z.; et al. Modulating Smart Mechanoluminescent Phosphors for Multistimuli Responsive Optical Wood. *Adv. Sci.* **2023**, *11*, e2305066. [[CrossRef](#)]
37. Tang, H.; Li, H.; Song, R.; Yang, Z.; Zhao, R.; Guo, Z.; Li, J.; Wang, B.; Zhu, J. Highly thermostable Ba₂Ln₂Ge₄O₁₃:Dy³⁺ (Ln = Y, Gd) phosphors: Synthesis and optical properties. *Ceram. Int.* **2023**, *49*, 31898–31906. [[CrossRef](#)]
38. Yang, Y.W.; Chen, Y.; Pei, P.; Fan, Y.; Wang, S.F.; Zhang, H.X.; Zhao, D.Y.; Qian, B.Z.; Zhang, F. Fluorescence-amplified nanocrystals in the second near-infrared window for in vivo real-time dynamic multiplexed imaging. *Nat. Nanotechnol.* **2023**, *18*, 1195–1204. [[CrossRef](#)] [[PubMed](#)]
39. Zhang, H.R.; Zheng, M.T.; Lei, B.F.; Xiao, Y.; Dong, H.W.; Liu, Y.L.; Liu, X.T.; Deng, J.J.; Deng, J.W.; Huang, Z.L. Preparation and Long-Lasting Phosphorescence Properties of BaAlSi₅N₇O₂: Eu²⁺. *ECS Solid State Lett.* **2013**, *2*, R16–R18. [[CrossRef](#)]
40. Poort, S.H.M.; Blokpoel, W.P.; Blasse, G. Luminescence of Eu²⁺ in barium and strontium aluminate and gallate. *Chem. Mater.* **1995**, *7*, 1547–1551. [[CrossRef](#)]

41. Setlur, A.A.; Comanzo, H.A.; Srivastava, A.M.; Beers, W.W. Spectroscopic Evaluation of a White Light Phosphor for UV-LEDs— $\text{Ca}_2\text{NaMg}_2\text{V}_3\text{O}_{12}:\text{Eu}^{3+}$. *J. Electrochem. Soc.* **2005**, *152*, H205. [[CrossRef](#)]
42. Fang, Y.-C.; Chu, S.-Y.; Kao, P.-C.; Chuang, Y.-M.; Zeng, Z.-L. Energy Transfer and Thermal Quenching Behaviors of $\text{CaLa}_2(\text{MoO}_4)_4:\text{Sm}^{3+}, \text{Eu}^{3+}$ Red Phosphors. *J. Electrochem. Soc.* **2011**, *158*, J1. [[CrossRef](#)]
43. Li, J.; Zhang, H.; Lei, B.; Qin, J.; Liu, Y.; Xiao, Y.; Zheng, M.; Sha, L. Luminescent properties of green long-lasting $\text{Ca}_8\text{Mg}(\text{SiO}_4)_4\text{Cl}_2:\text{Eu}^{2+}$, from $\text{Ca}_2\text{SiO}_4:\text{Eu}^{3+}$ and MgCl_2 at low temperature. *Phys. B Condens. Matter* **2013**, *430*, 31–35. [[CrossRef](#)]
44. Xia, Z.G.; Liu, R.S.; Huang, K.W.; Drozd, V. $\text{Ca}_2\text{Al}_3\text{O}_6\text{F}:\text{Eu}^{2+}$: A green-emitting oxyfluoride phosphor for white light-emitting diodes. *J. Mater. Chem.* **2012**, *22*, 15183–15189. [[CrossRef](#)]
45. Kozlova, L.O.; Ioni, Y.V.; Son, A.G.; Buzanov, G.A.; Murav'eva, G.P.; Kozerozhets, I.V. Low-Temperature Synthesis of Highly Dispersed Strontium Aluminate. *Russ. J. Inorg. Chem.* **2023**, *68*, 1744–1751. [[CrossRef](#)]

Disclaimer/Publisher's Note: The statements, opinions and data contained in all publications are solely those of the individual author(s) and contributor(s) and not of MDPI and/or the editor(s). MDPI and/or the editor(s) disclaim responsibility for any injury to people or property resulting from any ideas, methods, instructions or products referred to in the content.